PERGAMON

Journal of Structural Geology 25 (2003) 1713–1733

JOURNAL OF STRUCTURAL GEOLOGY

www.elsevier.com/locate/jsg

Brittle tectonics and pore-fluid conditions in the evolution of the Great Boundary Fault around Chittaurgarh, Northwestern India

Deepak C. Srivastava*, Amit Sahay

Department of Earth Sciences, Indian Institute of Technology, Roorkee 247667, India

Received 24 May 2001; received in revised form 18 December 2002; accepted 13 January 2003

Abstract

This paper aims at reconstructing paleostress history and deciphering the pore-fluid pressure conditions during the reactivation of a regional-scale fault. Paleostress analyses of the mesoscopic structures suggest that three successive events of reactivation on the Great Boundary Fault occurred in thrust-type, strike-slip type and thrust-type tectonic-settings, respectively. Whereas the pore-fluid pressure was supralithostatic during the first and third events of reactivation, it was sublithostatic during the second event. Each event of reactivation induced a fluid pressure gradient, which resulted in the focused and enhanced flow of syntectonic fluids within the high permeability locales, primarily fractures and faults.

Fluid inclusion study on strike-slip veins reveals that the syntectonic fluids were highly dense, Na–Ca–Cl brines of formational water origin. Stratigraphic evidence in favour of a 2-km-thick column of overburden above Kaimur sandstone beds implies that the strike-slip faulting occurred at 160–202 °C temperature and 53 MPa pressure. Variation in homogenization temperature reflects fluctuation in pore-fluid pressure during entrapment of syntectonic fluids and points to seismic pumping as a possible mechanism of fluid flow during faulting. High paleogeothermal gradient, obtained by fluid inclusion data, is ascribed to the high heat flow due to crustal stretching during the Proterozoic rifting, the basal and intermittent volcanism in the basin, and occurrence of Berach granite as the basement.

Keywords: Brittle tectonics; Pore-fluid conditions; Paleostress history

1. Introduction

Successive phases of reactivation on the large-scale faults commonly leave their imprints as distinct groups of mesoscopic structures that reveal the nature of reactivation and dynamic history of faulting (Zulauf and Duyster, 1997). Microscopic amounts of fluids, which are entrapped during tectonic evolution of faults and preserved as fluid inclusions, provide unique samples for constraining the physico-chemical conditions of faulting. In this paper, we trace the reactivation history of the Great Boundary Fault by paleostress analyses of the successive groups of brittle structures; and decipher the pressure–temperature, paleo-geothermal gradient, nature and source of syntectonic fluids, and variations in fluid pressure during faulting by micro-thermometric analyses of fluid inclusions (Vrolijk, 1987; Janssen et al., 1997).

2. The Great Boundary Fault

The Great Boundary Fault is an imbricate zone that comprises a series of steeply dipping reverse faults and intervening slices of sheared rocks in the Precambrian terrane of northwestern India (Sinha-Roy et al., 1995). Standing-out as the most conspicuous tectonic lineament in the northwestern Indian shield, this fault extends for more than 400 km from Machilpur in the northeast to a little south of Chittaurgarh in the southwest (Fig. 1). The Great Boundary Fault, barring a few exceptions, runs along the boundary of the Vindhyan basin. The latter contains basal volcanics, pyroclastic deposits at various stratigraphic levels and sediments deposited in a rift-valley type of tectonic setting (Chakraborty et al., 1996; Ram et al., 1996; Raza and Casshyap, 1996). That the Vindhyan basin represents an intracratonic rift is also substantiated by total magnetic intensity and Bouger anomaly profiles, showing crustal thinning below the basin (Mishra et al., 1996).

* Corresponding author.
E-mail address: dpkesfes@iitr.ernet.in (D.C. Srivastava).

0191-8141/03/$ - see front matter © 2003 Elsevier Science Ltd. All rights reserved.
doi:10.1016/S0191-8141(03)00012-9

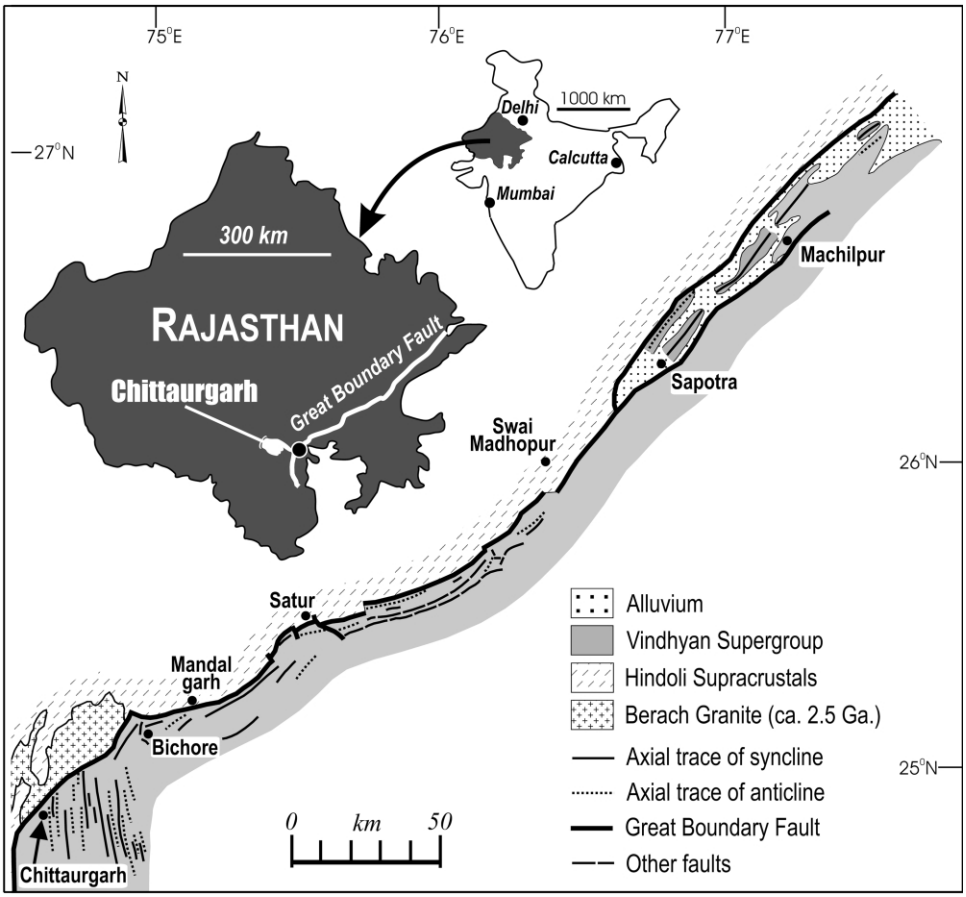

Fig. 1. Geological setting of the Great Boundary Fault (compiled from Banerjee and Singh, 1981; Prasad, 1984; Tiwari, 1995). Insets show the location of the Great Boundary Fault in India and Rajasthan.

In the southwestern sector, the Great Boundary Fault runs along the contact between the Archean basement, namely Berach granite, and the Paleo-Mesoproterozoic cover sequence belonging to the lower and middle parts of the Vindhyan Supergroup (Fig. 1). For most of its stretch in the central sector, the Great Boundary Fault runs close to the contact between the Archean/Paleoproterozoic supracrustals of the Hindoli Group and the Neoproterozoic sedimentary sequences belonging to the upper part of the Vindhyan Supergroup (Prasad, 1984). In the northeastern sector, the Great Boundary Fault comprises two sub-parallel faults, one of which cuts through the Neoproterozoic upper Vindhyan rocks and the other runs along the interface of the Hindoli supracrustals and upper Vindhyan rocks (Fig. 1).

Heron (1953) proposed that the Great Boundary Fault was developed during the uplift of the Aravalli ranges in the Mesozoic Era. Pascoe (1959) attributed its development to the folding of the Aravalli and Delhi Groups of rocks during Precambrian time. Fermor (1930) was the first proponent of the hypothesis that the Great Boundary Fault is a reactivated structure. His proposition that the Great Boundary Fault is a pre-Vindhyan structure, which has been reactivated as a reverse fault during and after the sedimentation of the Vindhyan Supergroup, has generally been accepted by the subsequent contributors (Iqbaluddin et al., 1978; Banerjee and Sinha, 1981; Prasad, 1984; Sinha-Roy et al., 1986; Verma, 1996). This study demonstrates that the tectonic history of the Great Boundary Fault comprises, at least, three successive events of reactivation, all of which occurred possibly during the Proterozoic era.

3. Geological setting

Our results are based on the observations around the Chittaurgarh region, where one of the best and most complete sections of the Great Boundary Fault is exposed in abundance (Fig. 1). It is only in and around the Chittaurgarh region that the granitic basement is juxtaposed against the cover rocks, and the large-scale folds in the cover-sequence trend oblique to the Great Boundary Fault (Fig. 1). Elsewhere, the axial-traces and limb-traces of the large-scale folds are mostly parallel to the Great Boundary Fault.

At Chittaurgarh, the Great Boundary Fault strikes NNE and represents a zone of intense deformation within the cover sequence of the Vindhyan Supergroup (Fig. 2a). This zone of deformation consists of: (i) a thin band (<100 m) of

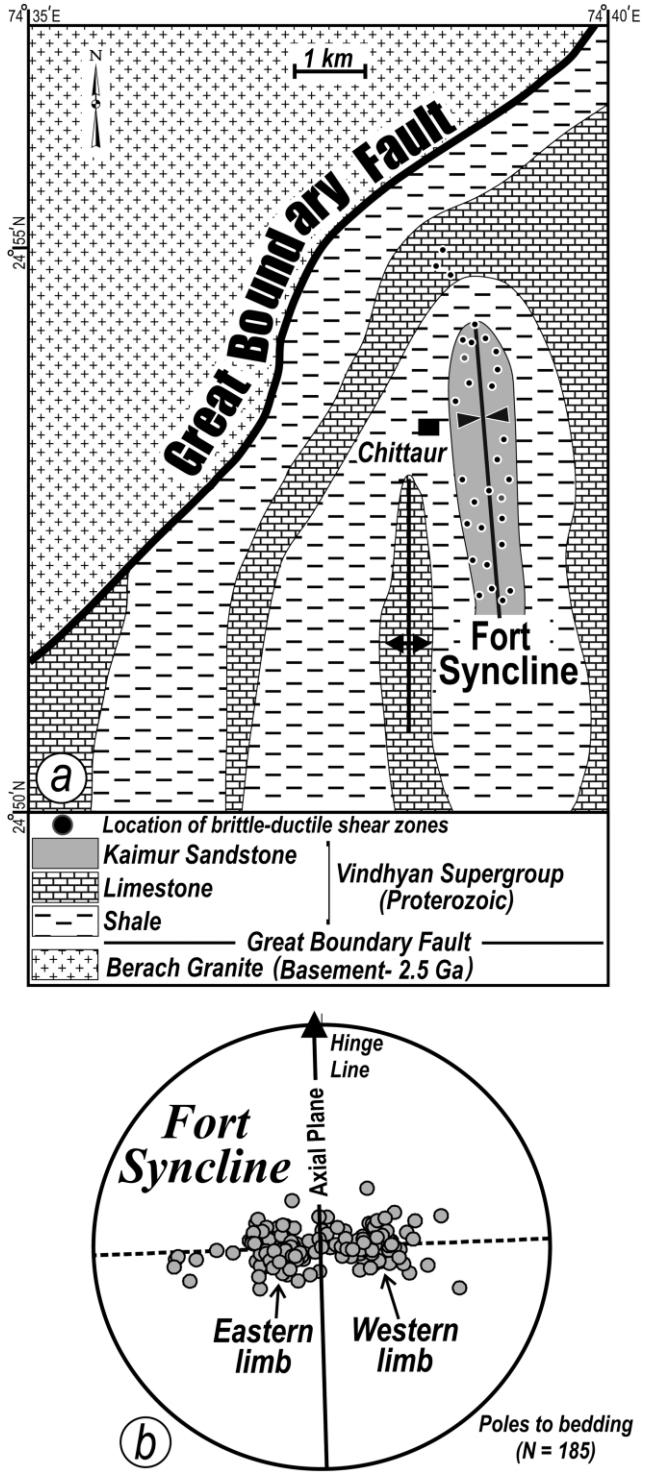

Fig. 2. (a) Geological map of the area around Chittaurgarh (lithological boundaries after Prasad, 1984). (b) Stereoplot reveals the open, upright, symmetric and non-plunging geometry of the Fort Syncline.

phyllonites, (ii) a thick zone (≈2 km) of abundant fractures, faults and en-échelon vein-arrays, and (iii) mesoscopic thrusts and thrust-related kink folds. The Vindhyan cover rocks, exposed in the vicinity of the Great Boundary Fault, are characteristically deformed into a series of open, N–S-trending and non-plunging folds (Fig. 2a and b). The basement represented by the Berach granite displays no perceptible imprints of the tectonic movements on the Great Boundary Fault.

4. Three phases of structures

The Vindhyan sedimentary sequence around Chittaurgarh bears imprints of the three successive phases of brittle deformation with each phase represented by a distinct group of dynamically compatible structures. Whereas the first phase structures are developed at both the mesoscopic and macroscopic scales, the second and the third phase structures are found to occur only at the mesoscopic scale. Structures of the first phase include: (i) large-scale folds typified by the Fort Syncline (Fig. 2a), (ii) mesoscopic kink bands on N–S-trending axes (Fig. 3a), and (iii) mesoscopic faults dipping at low angles (Fig. 3b). Structures of the second phase consist of mesoscopic fractures, brittle–ductile shear zones containing vein arrays, and strike-slip faults (Fig. 4a and b). Structures of the third phase include thrust faults and thrust-related kink folds on E–W-trending axes (Fig. 5a and b). Although large-scale folds belonging to the third phase do not occur in the Chittaurgarh area, such folds are observable in other parts of the Great Boundary Fault. For example, the E–W-trending kink fold around the Satur area, in the central sector of the Great Boundary Fault (Fig. 1), may represent a large-scale fold belonging to the third phase of deformation (Srivastava et al., 1999).

Three types of structural relationships are commonly observed amongst the structures belonging to different phases. These include: (i) the orientations of the mesoscopic scale second phase structures are highly consistent in all the segments of large-scale folds belonging to the first phase, (ii) thrust faults of the third phase offset and drag the veins of the second phase, and (iii) the kink folds belonging to the first- and third- phases interfere in such a manner that the axes of first phase kink folds are rotated from N–S, through NE–SW, to E–W.

5. First phase structures

5.1. Kink bands on N–S axes

Numerous compressional type kink bands occur as parasitic folds at the limbs of the large-scale first phase folds, exemplified by the Fort Syncline (Fig. 3a). These kink bands occur in two conjugate sets, which are characterized by top-to-the-west and top-to-the-east sense of movement, respectively. The axes of kinks in both sets are non-plunging and N–S-trending. On the eastern limb of the Fort Syncline, an axial plane cleavage and a bedding/cleavage intersection lineation are developed parallel to the kink planes and kink axes, respectively.

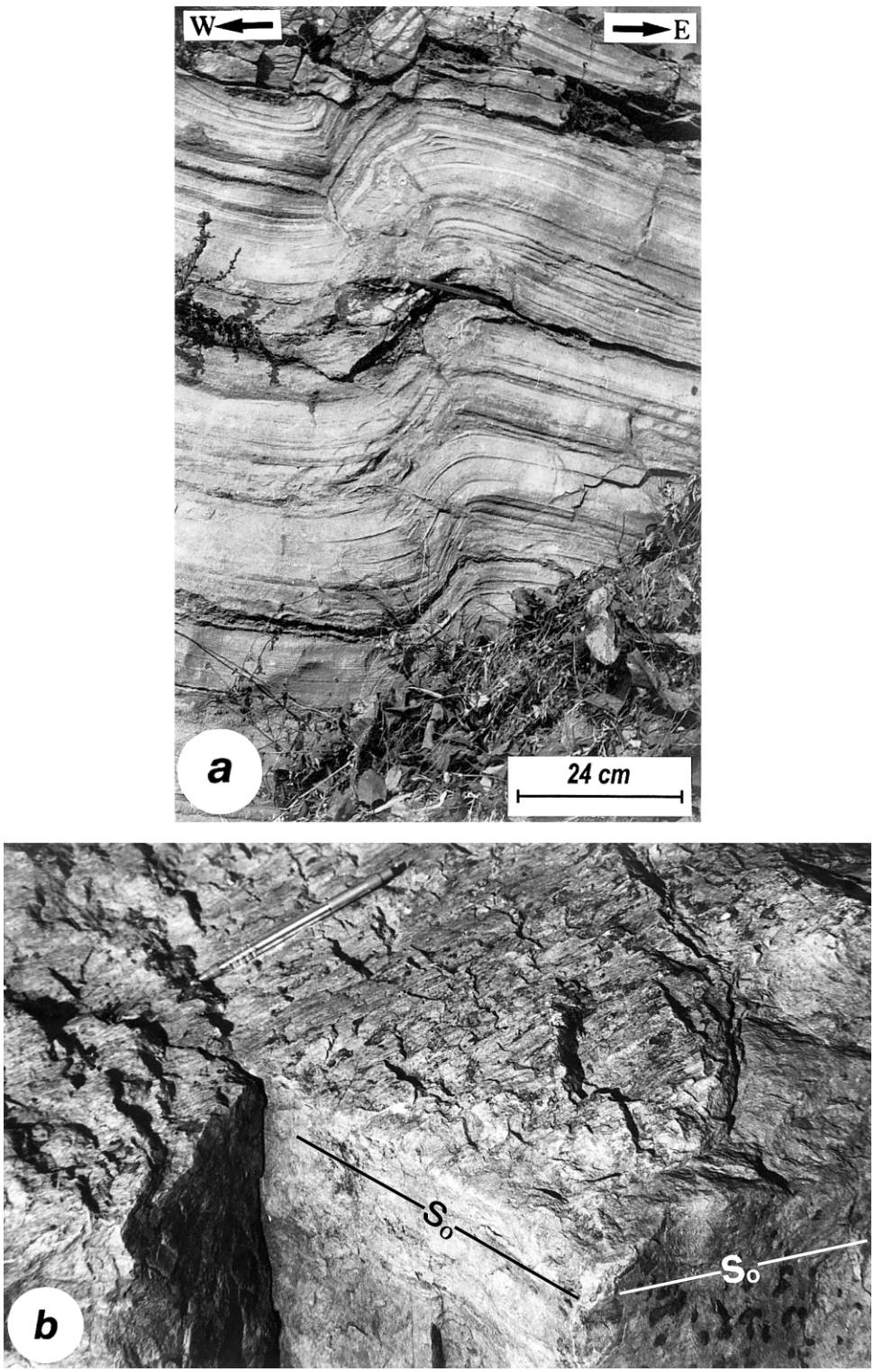

Fig. 3. First phase structures. (a) Profile section of a top-to-the-west kink band in the limestone beds. The kink axis is horizontal/N–S. (b) A low-angle thrust fault cutting through the Kaimur sandstone bed on the western limb of the Fort Syncline. S_0—trace of the bedding surface. Pencil parallels the slicken/groove lineations indicating an up-dip movement of the missing block.

As the conjugate pairs of the first phase kink bands possess a characteristic orthorhombic symmetry, these structures qualify for the paleostress analysis by the method proposed by Ramsay (1962). The results of paleostress analysis reveal that these kink bands were developed in a thrust-type tectonic setting, such that the maximum and the intermediate principal stresses, σ_1 and σ_2 were horizontal and trending E–W and N–S, respectively, and the

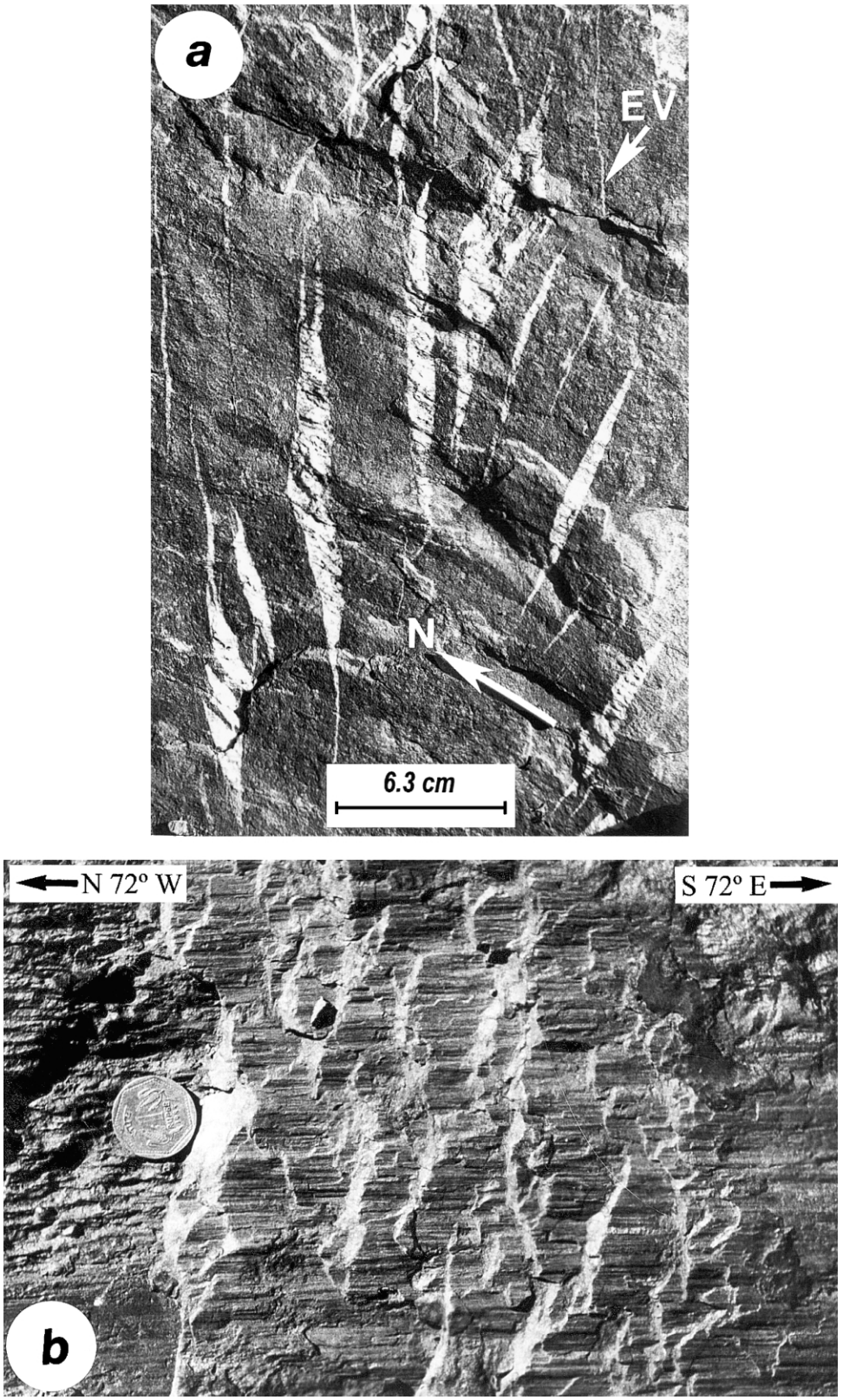

Fig. 4. Second phase structures. (a) Plan view of a conjugate pair of vein arrays cutting the Kaimur sandstone bed on the eastern limb of the Fort Syncline. Individual veins and array boundaries are sub-vertical. Thin extension veins (EV) in the upper part of the photograph bisect the dihedral angle between the complementary arrays. Note that almost all fibres are parallel. (b) A dextral strike-slip fault in the Kaimur sandstone bed on the western limb of the Fort Syncline. The fault-surface is vertical and the slicken/groove lineations are sub-horizontal.

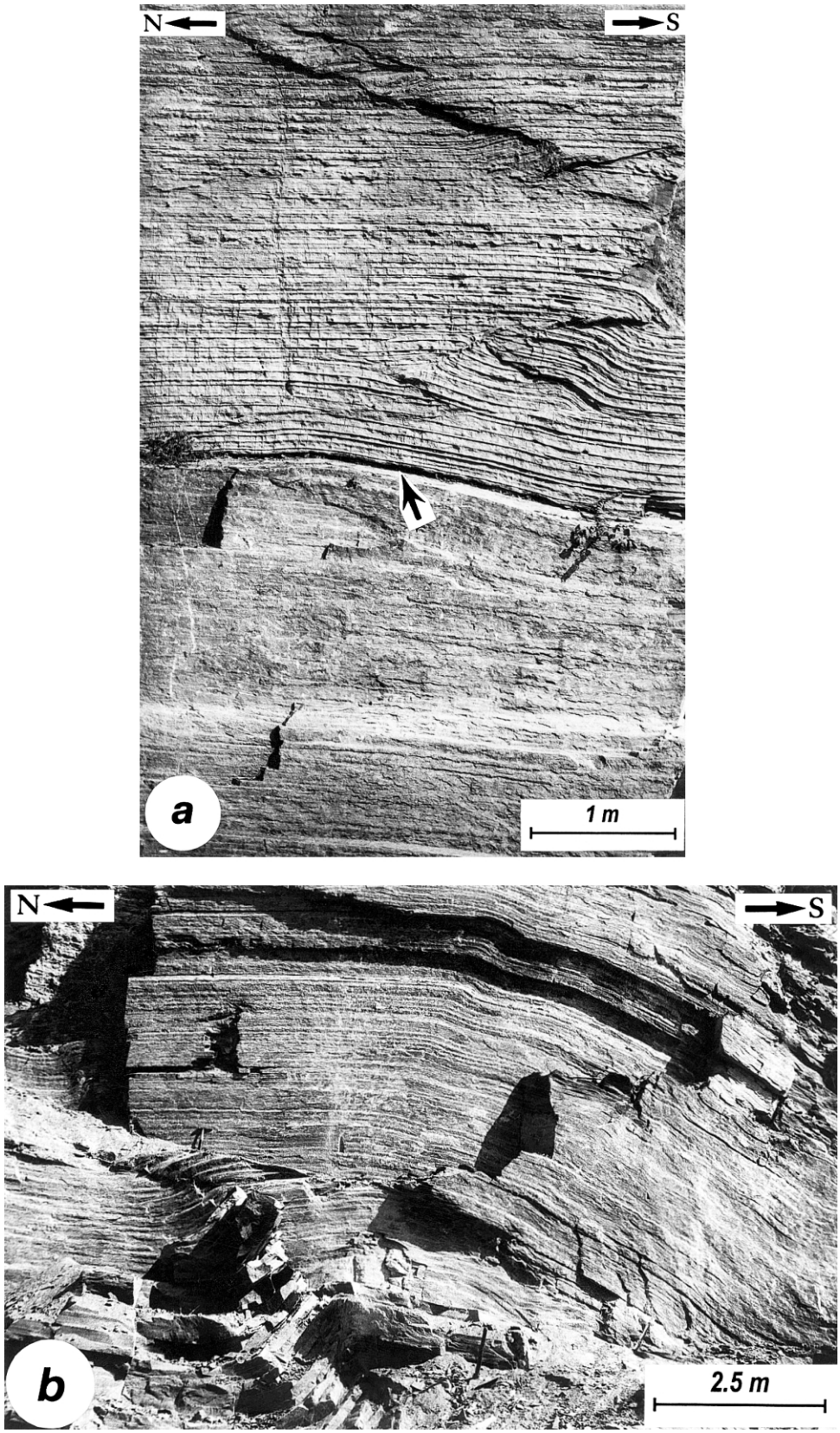

Fig. 5. Third phase structures. (a) Profile view of kink bands and the associated thrust faults in the limestone beds above the decollement surface (pointed by arrow). The kink axes are horizontal/E–W. (b) Top-to-the-north thrust and associated kink band in the limestone beds (profile view).

minimum principal stress, σ_3, was vertical (Fig. 6a). That the symmetry of these kink bands is orthorhombic is reaffirmed by the results of paleostress analyses, which show that the intermediate and minimum principal stresses, σ_2 and σ_3, parallel the kink axes and the pole to external foliation, respectively (Fig. 6a).

5.2. Low angle faults

Faults belonging to the first phase dip characteristically at shallow angles $\leq 45°$, and these structures are best exposed in the Kaimur sandstone beds on the western limb of the Fort Syncline (Fig. 3b). The fault surfaces display profuse lineations in the form of ridges, grooves and slicken-lines implying a consistent top-to-the-up-dip sense of movement. Only those faults that indicate unambiguous sense and direction of movement are considered for the paleostress analysis.

These faults are treated by both graphical and numerical methods, such as the P–T axes method and the direct inversion method, respectively (Turner, 1953; Angelier, 1990, 1994). Three basic assumptions that are implicit in the application of the P–T axes method can be enumerated as: (i) the intermediate principal stress σ_2 lies on the fault plane at an angle of 90° from the slip-lineation, (ii) the movement plane contains the slip-lineation, maximum principal stress σ_1, minimum principal stress σ_3, and the pole to the fault plane, and (iii) on the movement plane, the σ_1-axis lies at an angle of 45°-(ϕ/2) from the slip direction, measured in the direction of movement of the footwall, where ϕ is the angle of internal friction. In this work, ϕ is assumed to be equal to 30°, which is the common value for the angle of internal friction in most rocks (Ragan, 1985).

The direct inversion method is based on the principle of determining a stress tensor by minimizing the angle between the theoretically calculated direction of maximum shear stress and the practically observed slip-lineation (Angelier, 1994). This method yields a reduced stress tensor with four components; namely, the three orientations of the principal stresses, and the shape factor Φ, which is the ratio of two differential stresses $(\sigma_2 - \sigma_3)/(\sigma_1 - \sigma_3)$. One distinct merit of the direct inversion method is its independence from the condition that the intermediate principal stress σ_2 must lie in the fault plane. The other merit is its applicability to faults that are developed as fresh ruptures, as well as to those faults that are reactivated along pre-existing discontinuities in rocks. Furthermore, the quality of results yielded by this method can be evaluated quantitatively by parameters COH, ANG and RUP, which are acronyms for quality estimators in the TENSOR program of Angelier (1994). For a given population of faults, COH indicates the total percentage of those faults that agree with the stress solution. Both ANG and RUP indicate the misfit angle, i.e. angle between the theoretically calculated direction of maximum shear stress and the practically observed direction of the slip lineation. RUP is considered a better indicator of the quality of stress solution than ANG because it not only describes the misfit angle but also indicates the magnitude of relative shear stress.

Results from both the P–T axes and the direct inversion methods are consistent with a stress configuration with E–W/horizontal maximum principal stress σ_1, N–S/horizontal intermediate principal stress σ_2, and a vertical minimum principal stress σ_3 (Fig. 6b and c). These results imply that the low-angle faults formed in a thrust-type tectonic regime (Fig. 6b and c). The principal stresses yielded by the fault-slip analyses of the first phase faults match in orientation the respective principal stresses obtained by

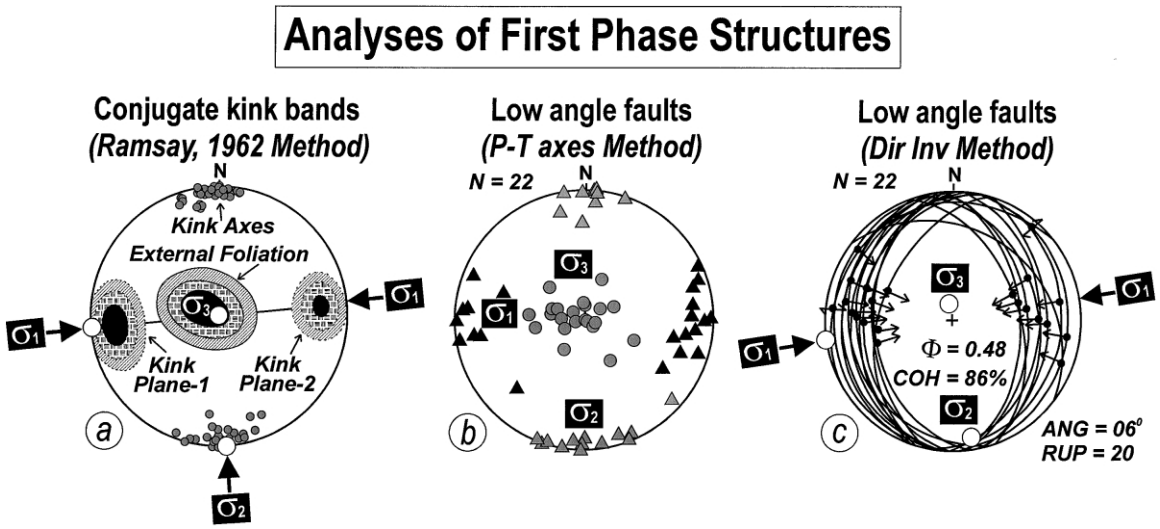

Fig. 6. Paleostress analyses of the first phase structures. (a) Kink plane-1 and kink plane-2 are complementary sets of conjugate pairs. Contouring by Kamb method. For kink plane-1, $N = 31$ and contours at $5-10-15\sigma$; $\sigma = 1.6$. For kink plane-2, $N = 58$ and contours at $7-14-21\sigma$; $\sigma = 1.3$. For external foliation, $N = 50$ and contours at $7-14-21\sigma$; $\sigma = 1.27$. For kink axes, $N = 58$. White circles—principal stresses (b) and (c) Stress analysis of the low angle faults. (b) P–T axes method; black triangle—σ_1-axis; grey triangle—σ_2-axis; grey circle—σ_3-axis. (c) Direct inversion method; great circle—fault surface; arrow on black dot—direction and sense of movement on the fault surface, white circles—principal stresses. See text for the definition of Φ, COH, RUP and ANG.

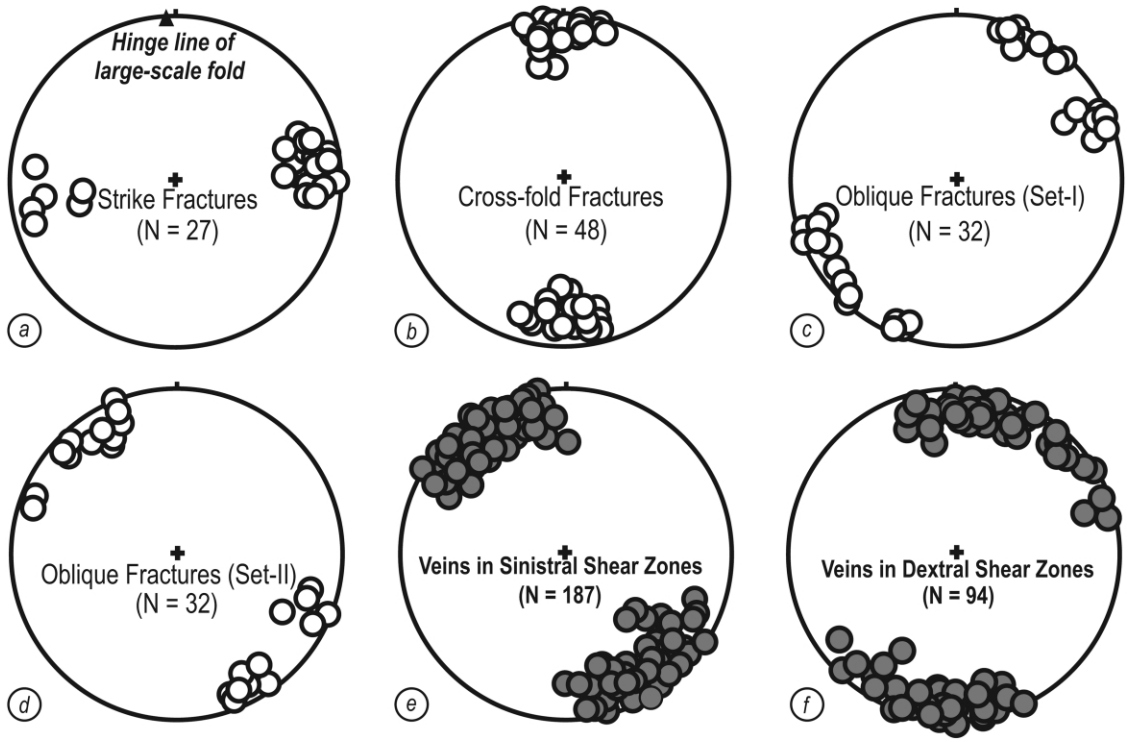

Fig. 7. Stereoplots showing the orientations of second phase structures. (a)–(d) Fractures. (e) and (f) Veins. The orientations of the oblique fractures (set-II) and veins in the sinistral shear zones are identical (cf. (d) and (e)). Similarly, the orientations of the cross-fold fractures and oblique fractures (set-I) are identical to the orientation of the veins in the dextral shear zones (cf. (b), (c) and (f)). Mesoscopic veins corresponding to strike fractures are absent.

the independent analysis of the conjugate kink bands. Such a dynamic compatibility between these structures substantiates the interpretation that the low-angle faults, N–S-trending kink bands and the large-scale folds, such as the Fort Syncline, were all developed during a common deformation event.

The fault-slip analyses do not reveal absolute magnitudes of the principal stresses. The direct inversion method, however, yields the relative values of the principal stresses in terms of a shape factor Φ. As the direct inversion method applied to low-angle faults reveals that the value of Φ is close to 0.5, it is evident that the first phase of deformation occurred in a plane-deviatoric state of stress, i.e. $\sigma_2' = 0$. It is the consequence of such a plane-deviatoric state of stress that the first phase faults at Chittaurgarh are pure dip-slip thrusts (Fig. 3b).

6. Second phase structures

Fractures, faults and en-échelon veins belonging to the second phase cut through the first phase structures throughout the study area. Furthermore, the second phase structures are consistent with respect to orientation, regardless of the variation in the orientation of bedding-surface due to the first phase folding. Finally, all the second phase structures are either vertical or dip at steep angles.

6.1. Fractures

Fractures cutting through the limestone–shale–sandstone sequence of the Fort Syncline are characterized by sub-vertical dips and lack of features such as plumose markings, arrest lines or slicken-lineations. Based on the relative orientation with respect to the N–S-trending hinge lines of the large-scale folds, these fractures can be classified into four sets: (i) a strike-set that consists of N–S-striking fractures, (ii) a cross-fold set that consists of E–W-striking fractures and, (iii) and (iv) the two sets of oblique fractures; namely, oblique set-I and oblique set-II striking NNW–NW and NNE–NE, respectively (Fig. 7a and d). Lack of consistent crosscutting and abutting relationships amongst the fractures of different set points to their broadly synchronous origin.

6.2. Brittle–ductile shear zones

Conjugate pairs of brittle–ductile shear zones containing en-échelon vein-arrays cut through both the limbs and the hinge zone of the Fort Syncline (Fig. 4a). The direction of movement on these shear zones is sub-horizontal, because the line of intersection between the shear zone-boundary and the veins is invariably sub-vertical. At some outcrops, two or more contiguous shear zones occur in different orientations but imply the same sense of relative movement. Inconsistent overprinting relationships amongst such

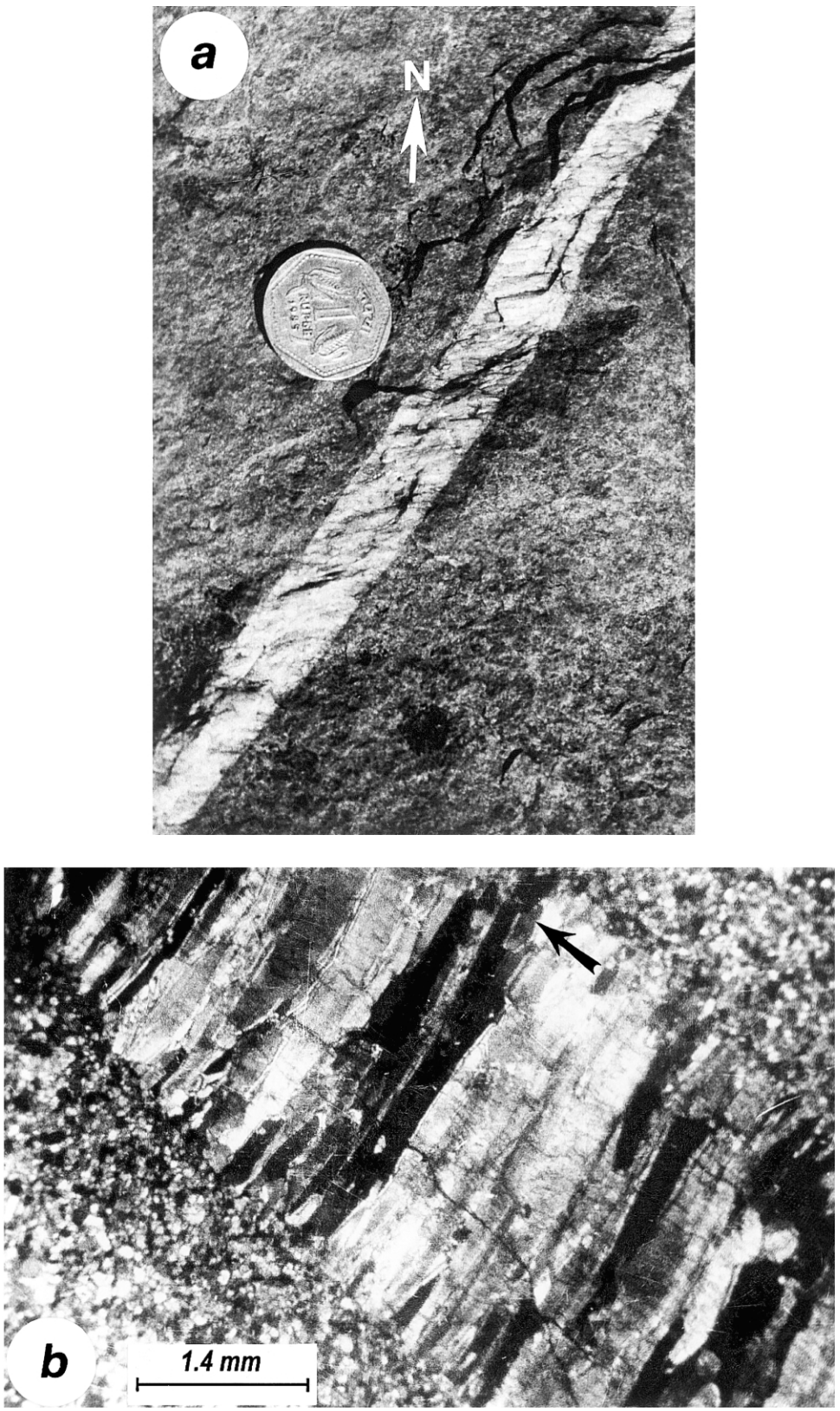

Fig. 8. Vein textures. (a) Plan view of a stretched crystal fibre type of vein. The vein infilling is characteristically made-up of rectilinear fibres that are oblique to the vein margins. (b) Wall-to-wall optical continuity in the fibres in a stretched crystal fibre type of vein. One of the optically continuous fibres is indicated by the arrow.

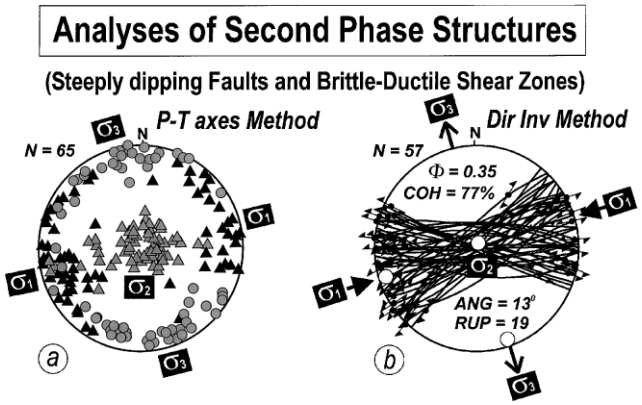

Fig. 9. Paleostress analyses of the second phase structures. (a) P–T axes method. Black triangle—σ_1; grey triangle—σ_2; and grey circle—σ_3. (b) Direct inversion method. Great circle—fault plane/shear zone; half arrows on dot—sense and direction of movement. White circles—principal stresses. See text for the definition of Φ, COH, RUP and ANG.

diversely oriented shear zones point to their coeval development as hybrid extensional-shear fractures. The angle between the veins and the shear zone-boundary ranges between 10 and 58°, although the modal value of this angle is 35–45° in most of the arrays.

The orientational and geometrical similarities between the en-échelon veins and fractures point to their dynamically compatible nature. Whereas the fractures of the cross-fold set and the oblique set-I match in orientation with the veins in the dextral shear zones, the fractures of the oblique set-II parallel the veins in the sinistral shear zones (compare Fig. 7b and c with f; and Fig. 7d with e). Strike fractures are, in general, barren at the mesoscopic-scale.

Rectilinear fibres of quartz and calcite constitute the bulk of the infillings of veins cutting through the sandstone and limestone beds, respectively. In general, these fibres are inclined at 60–80° with respect to the vein-margin and stretch in a characteristic optical continuity from one margin of the vein to the other (Fig. 8a and b). Most of these veins are of hybrid extensional-shear origin. In the rare veins that are of predominantly shear origin, the angle between fibres and vein-boundary is typically low, $\leq 15°$, although presumably there is some amount of extension across these veins, as well. Microstructures such as, the 'stretched' crystal geometry of fibres, the occurrence of wall-parallel fluid inclusion bands and the irregular geometry of contacts between adjacent fibres imply that 'crack-seal' rather than 'taber-growth' model is the favoured mechanism of vein development in the study-area (Ramsay, 1980; Means and Li, 2001).

6.3. Sub-vertical faults

Faults belonging to the second phase are characterized by sub-horizontal slip-lineations and sub-vertical or steeply-dipping fault surfaces (Fig. 4b). These faults occur in two conjugate sets that imply dextral and sinistral sense of relative movements. The dextral and sinistral faults are characteristically parallel to the dextral and the sinistral brittle–ductile shear zones, respectively. The sense and direction of relative movement is invariably consistent on those faults and shear zones that are parallel to each other.

6.4. Paleostress analyses of the second phase structures

As the brittle–ductile shear zones and steeply-dipping faults are similar with respect to their orientations and kinematics, these two types of structures are grouped together for dynamic analysis by fault-slip techniques. Only those brittle–ductile shear zones that contain planar veins of simple geometry are considered for the fault-slip analysis. Shear zones containing sigmoidal, or geometrically complex veins, are not considered for the paleostress analysis because of the concentration of a significant amount of strain in such zones. The direction of movement on the shear plane is perpendicular to the line of intersection of the veins and the shear

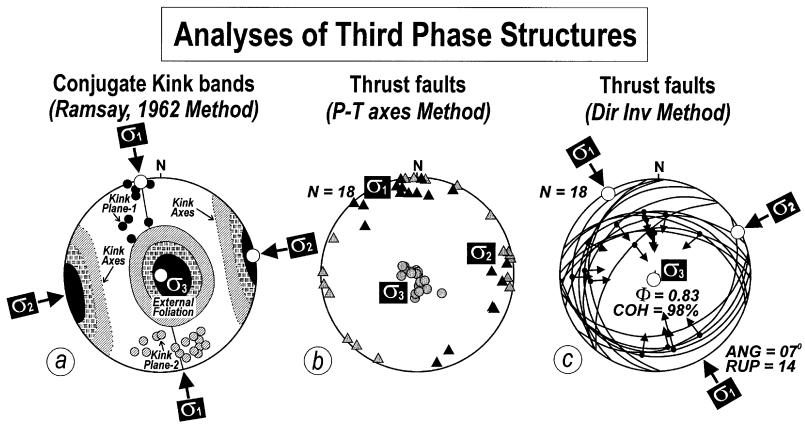

Fig. 10. Paleostress analyses of the third phase structures. (a) Kink plane-1 and kink plane-2 are the complementary sets of conjugate pairs. Grey circles—poles to kink plane-1; $N = 8$. Hatched circles—poles to kink plane-2; $N = 16$. For external foliation, $N = 33$ and Kamb contours at 5–10–15σ; $\sigma = 1.18$. For kink axes, $N = 39$ and Kamb contours at 6–12–18σ; $\sigma = 1.22$. White circles—principal stresses. (b) and (c) Stress analysis of the thrust faults. (b) P–T axes method; black triangle—σ_1; grey triangle—σ_2; grey circle—σ_3. (c) Direct inversion method; great circle—fault plane; arrow on dot—direction and sense of movement. White circles—principal stresses.

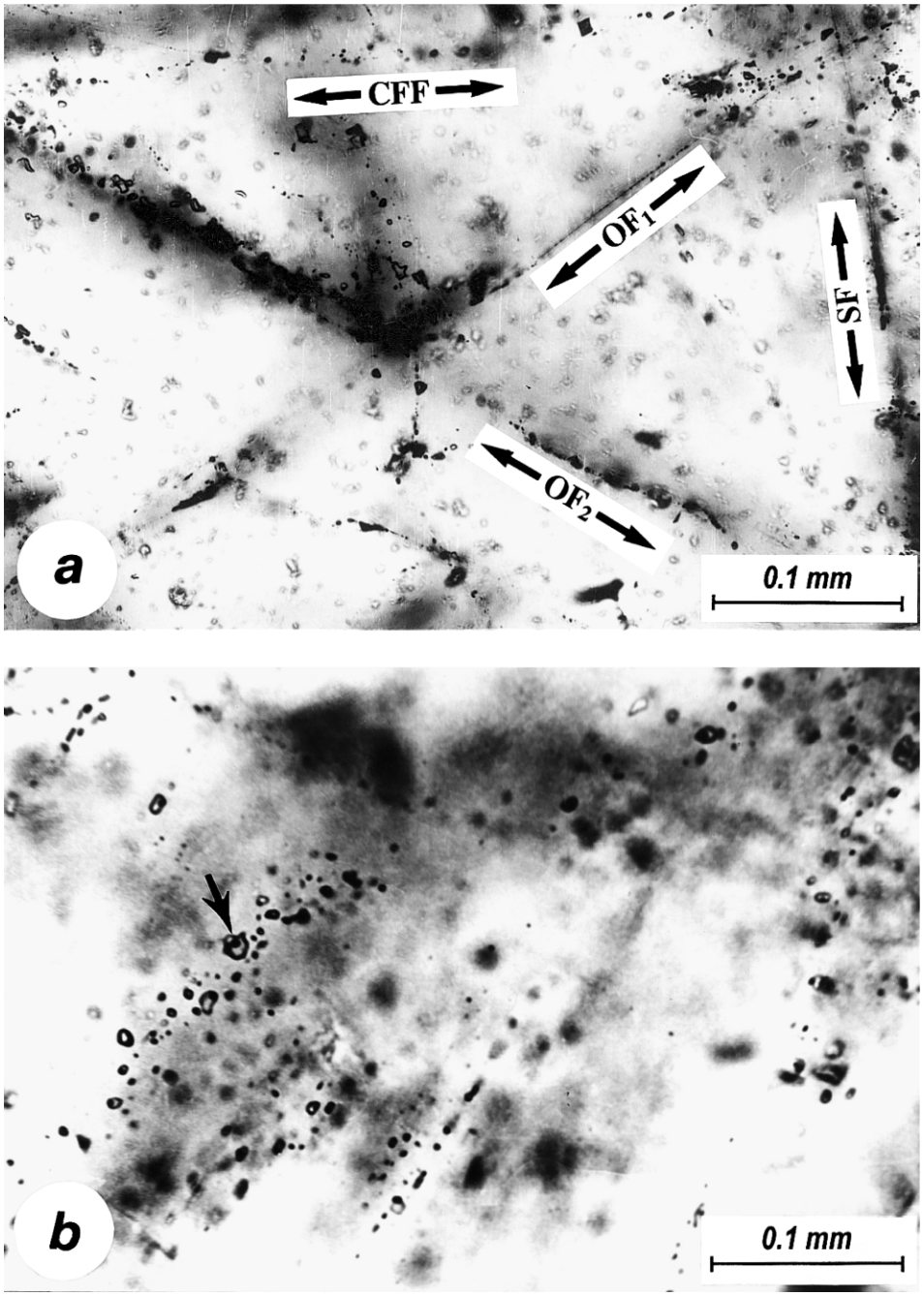

Fig. 11. Mode of occurrence of the fluid inclusions. (a) Four sets of secondary fluid inclusions occur in the transgranular arrays paralleling cross-fold fractures (CFF), strike fractures (SF), oblique fractures of set-I (OF_1) and oblique fractures of set-II (OF_2). (b) Arrays of secondary fluid inclusions show the presence of liquid phase and vapour phase at the room conditions (marked by arrow).

zone-boundary (Srivastava et al., 1995). The relative sense of movement is determined by the angular relationship between the veins and shear zone-boundary.

Results from both the P–T axes and the direct inversion methods consistently reveal that the second phase structures were developed in a strike-slip type tectonic-setting (Fig. 9a and b). This tectonic regime comprised a horizontal maximum principal stress σ_1 trending ENE–WSW, a vertical intermediate principal stress σ_2, and a horizontal minimum principal stress σ_3 trending NNW–SSE. As the second phase structures occur in conjugate sets, these are independent of relative values of the principal stresses and the value of Φ yielded by the direct inversion method is insignificant in this case.

7. Third phase structures

7.1. Kink folds on E–W axes and thrust faults

The third phase structures are developed exclusively in

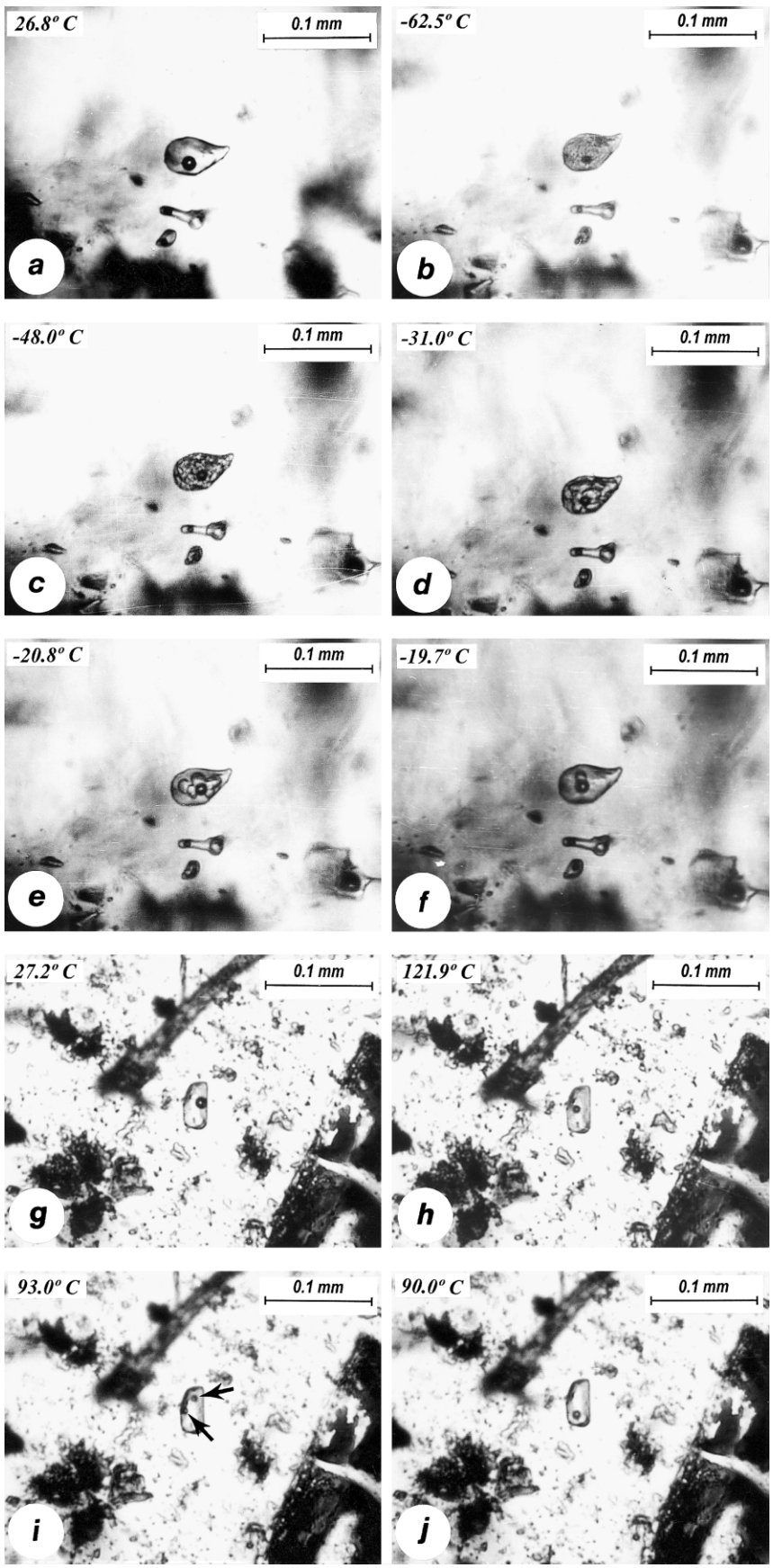
26.8° C
0.1 mm
a
-62.5° C
0.1 mm
b
-48.0° C
0.1 mm
c
-31.0° C
0.1 mm
d
-20.8° C
0.1 mm
e
-19.7° C
0.1 mm
f
27.2° C
0.1 mm
g
121.9° C
0.1 mm
h
93.0° C
0.1 mm
i
90.0° C
0.1 mm
j

those beds that are exposed in the vicinity of the basement-cover contact. Whereas structures of the first and the second phases are abundant on both limbs of the Fort Syncline, those of the third phase are characteristically absent in domains distant from the contact of the Berach granite basement and the Vindhyan cover sediments.

Although the kink folds of the third phase are also compressional in type and occur as conjugate pairs, they are distinct from the first phase kinks in the following respects. (i) Whereas the axes of the first phase kinks trend N–S, the axes of the third phase kinks trend E–W or ENE–WSW. (ii) The conjugate pairs of the first phase kinks imply top-to-the-east and top-to-the-west sense of relative movements, respectively. In contrast, the conjugate pairs of the third phase kinks imply top-to-the-north and top-to-the-south sense of relative movements, respectively. (iii) The first phase kinks are not directly associated with mesoscopic thrust faults. In contrast, the third phase kinks are almost always associated with the mesoscopic-scale thrust faults and their geometry is demonstrably controlled by the geometry of the thrust faults (Fig. 5a and b). Thin carbonate veins along such thrust surfaces trace the mesoscopic-scale flat and ramp and duplex structures, which occur in common association with the third phase kinks.

7.2. Paleostress analyses of the third phase structures

Independent paleostress analyses of the kink folds and the thrust faults belonging to the third phase reveal that these two types of structures are dynamically compatible (Fig. 10a and c). The stress configuration responsible for development of the third phase structures comprised a horizontal σ_1-axis trending NNW–SSE, a horizontal σ_2-axis trending ENE–WSW, and a vertical σ_3-axis. As the value of Φ for the third phase thrust faults is close to one ($\Phi = 0.88$), it can be inferred that the effective intermediate principal stress σ_2' was approximately equal to the effective maximum principal stress σ_1', and the state of stress approached axial extension ($\sigma_1' \approx \sigma_2' > 0$).

8. Analysis of syntectonic fluids

Numerous veins of quartz and calcite occur within the strike-slip shear zones, belonging to the second phase. Freezing–heating experiments were performed on the fluid inclusions within the quartz infillings. Most of these fluid inclusions occur in transgranular arrays paralleling the cross-fold fractures, strike fractures and the two sets of the oblique fractures (Fig. 11a). Of the two phases present in all the fluid inclusions at the ambient temperature, the liquid phase and vapour phase occupy about 80–90% and 10–20% by volume, respectively (Figs. 11b and 12a and g). Microstructural studies show that these fluid inclusions are localized along the microfractures formed during the development of veins by crack-seal process (Ramsay, 1980; Roedder, 1984; Lespinasse and Pecher, 1986; Lespinasse, 1999). Such types of fluid inclusions bear a great potential for deciphering not only the composition of syntectonic fluids but also the pressure, temperature and depth of overburden/paleogeothermal gradient during faulting (Srivastava and Engelder, 1990).

More than 150 fluid inclusions, occurring in the doubly-polished wafers of 10 samples, were analyzed on a Reynold's fluid inclusion stage—a modified version of the USGS gas flow type fluid inclusion stage. Representative examples of important phase changes observed during the freezing–heating experiments are shown in Fig. 12a–j. As most of the fluid inclusions were small ($\leq$10–15 μm), cycling technique was used extensively for detection of the phase changes. By mapping each chip of the doubly-polished wafers in detail, it was possible to perform both freezing and heating experiments on the same fluid inclusion in 104 cases. Though tedious, the approach yielded a paired set of freezing–heating data that are useful for making distinctions between different populations of fluid inclusions and inferring the cause of scattering in the paired data set (Fig. 13a).

It was, however, not always possible to obtain a paired freezing–heating data on each and every fluid inclusion. For example, total homogenization could not be achieved due to leakage or decrepitation of fluid inclusions during some of the heating experiments. Similarly, distinct phase changes could not be observed in very small ($\leq$4 μm) fluid inclusions during the freezing experiments. As the unpaired data cannot be plotted on a Cartesian graph, these are grouped together with the paired data and represented on separate frequency histograms for each type of the phase change (Fig. 13b–f). Statistical means, or modes, that are used traditionally to represent temperatures of phase changes, nevertheless, are less reliable indicators of the fluid inclusion population than clusters on the paired data plots. One limitation in considering the statistical mode is

Fig. 12. (a)–(f) A typical sequence of phase changes during the freezing experiments. (a) A two-phase fluid inclusion at room conditions. (b) The fluid inclusion shows pale-brown appearance, 'mosaic texture' and the collapsed vapour bubble at −62.5 °C. (c) 'Orange-peel' texture indicating eutectic melting at a temperature close to −48 °C. Two types of solid phases; namely, fine grained euhedral hydrohalite and coarse grained rounded ice crystals, are observed at this stage. (d) Most of the hydrohalite crystals have melted at −31 °C. (e) A few ice crystals that remain after the melting of all the hydrohalite crystals. Note that the inclusion is more clear, and the vapour bubble is bigger and more rounded as compared with the stage shown in (d). (f) The last crystal of ice is close to melting at −19.7 °C. (g)–(j) A typical sequence of phase changes during the heating runs. (g) A two-phase fluid inclusion at room conditions. (h) The vapour bubble is close to homogenization at 121.9 °C. It eventually homogenized at 125 °C. (i) Two vapour bubbles, indicated by the arrows, pop-up at 93 °C during the post-homogenization cooling. (j) The two popped-up vapour bubbles amalgamate into one bubble at 90 °C.

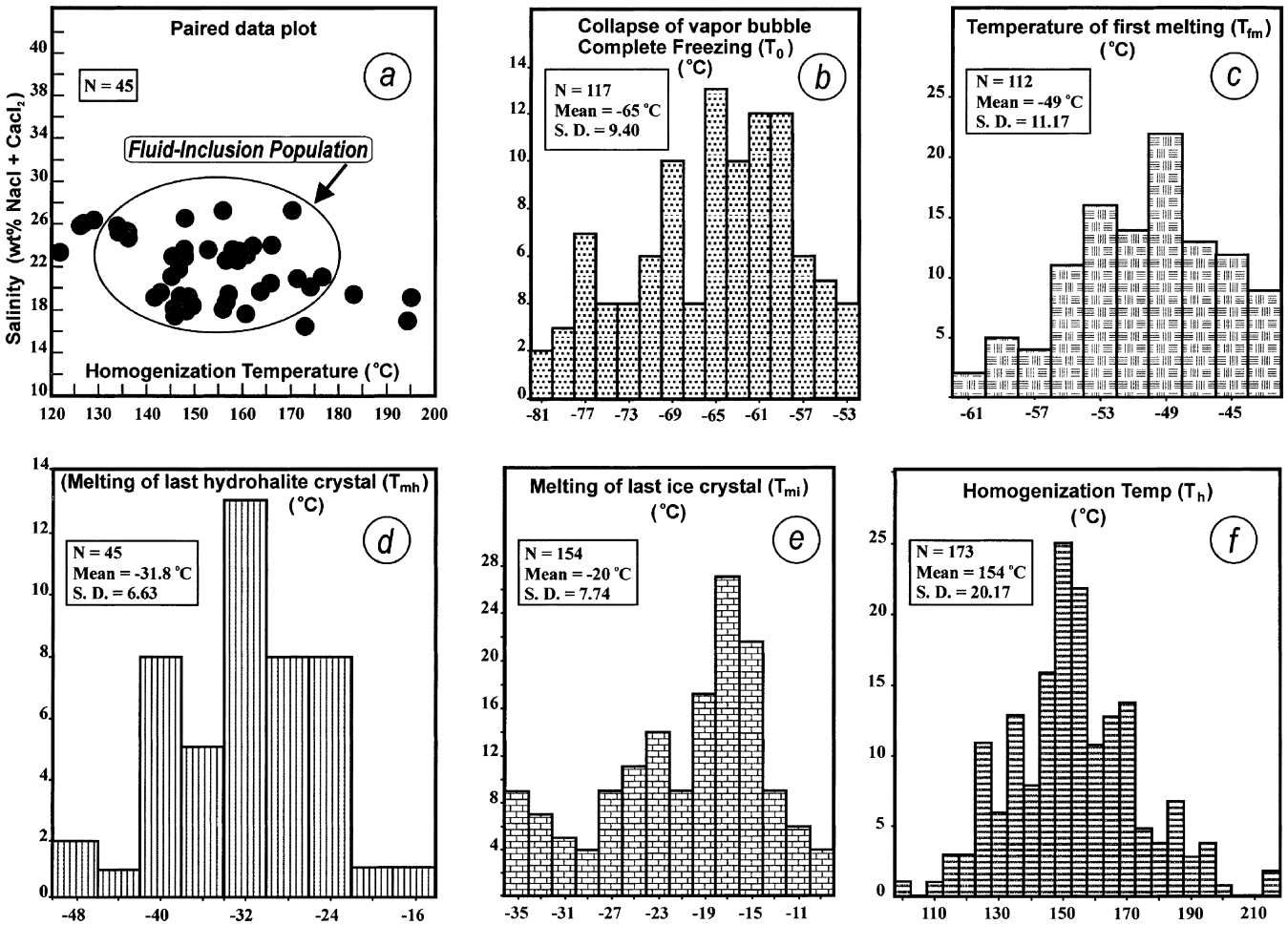

Fig. 13. (a) Paired plots between the salinity and homogenization temperature for the same fluid inclusion. These data are obtained from those fluid inclusions that show the melting of both the hydrohalite and the ice. The representative population is encircled. (b)–(e) Histograms for the temperatures at which important phase changes occur during the freezing experiments. The temperature of collapse of vapour bubble (T_0) shown in (b) has no physico-chemical significance and the temperature of first melting (T_{fm}) shown in (c) is close to or slightly above the eutectic temperature (T_e). (f) Histogram for the temperature (T_h) at which the vapour phase homogenizes into the liquid phase.

that the frequency of a particular class-interval may be spuriously high due to mixing of data from two or more populations. Furthermore, only one variable is taken into account in plotting a histogram. Besides being more reliable for discriminating between different fluid inclusion populations, the paired data plots often display such patterns that are characteristic of the fluid evolution path (Goldstein and Reynolds, 1994).

8.1. Freezing experiments

Complete freezing of the inclusions was marked by the collapse of the vapour bubble with a sudden jerk at temperature T_0 (Fig. 13b). Upon slow and continued warming, the fluid inclusions turned pale-brown and showed a 'mosaic texture' due to metastable reaction or solid state recrystallization (Fig. 12b). This phenomenon occurred typically at a temperature that was, at least, 10 °C lower than the eutectic temperature (Davis et al., 1990; Goldstein and Reynolds, 1994). With continued warming, the fluid inclusions showed an extremely granular or 'orange-peel' texture signaling the commencement of melting of the solid phases (Fig. 12c). The temperature (T_{fm}) at which this texture is observed is close to or slightly above the eutectic temperature (T_e) which, in turn, is indicative of the type of salts present within the brines. At this stage, most fluid inclusions contained a mixture of two types of solid-phases: (i) fine-grained and euhedral hydrohalite crystals, NaCl. $2H_2O$, and (ii) coarse-grained and rounded ice crystals H_2O (Fig. 12c). A slight change in the shape of the vapour bubble with a sudden jerk and a noticeable increase in the clarity of fluid inclusion marked the melting of the last crystal of hydrohalite at the temperature T_{mh}. The actual melting of the last hydrohalite crystal was, however, only rarely observed. Finally, ice was found to be the only solid-phase that remained in the fluid inclusion (Fig. 12d and e). The last crystal of ice was distinctly noticed in most of the fluid inclusions and its melting temperature T_{mi} could be recorded with an accuracy of ± 0.1 °C (Fig. 12f).

8.2. Heating experiments

During the gradual heating of the fluid inclusions, the vapour bubble progressively decreased in size and was eventually homogenized into the liquid-phase at homogenization temperature T_h (Fig. 12g and h). No fluid inclusion was ever found to homogenize into the vapour-phase. In order to minimise the effects of necking and stretching, homogenization temperatures were measured only on those fluid inclusions that showed a consistent liquid/vapour ratio at room temperature. Subsequent to homogenization, the vapour bubble returned after several tens of degrees of cooling, and in some cases, the vapour bubble showed up only after a couple of days' cooling at room temperature. In a few fluid inclusions, the vapour bubble returned in two small parts that amalgamated quickly to form a single bubble (Fig. 12i and j). All these phenomena are considered to indicate the metastable nature of the entrapped fluid. Table 1 gives a summary of the microthermometric observations and representative temperatures of the significant phase changes.

8.3. Fluid inclusion population

Final melting of both the solid phases, that is, hydrohalite and ice, could be detected during the freezing experiments on 45 inclusions. Using the *CalcicBrine* program of Naden (1996), bulk salinities of these fluid inclusions are calculated and plotted against their respective homogenization temperatures (Fig. 13a). The paired plots of salinity versus homogenization-temperature as well as the histograms reveal that only one dominant population of the fluid inclusions is present in spite of the large scatters (cf. Fig. 13a and b–f). The scatter in salinity of fluids is within the standard deviation of the data (Fig. 13a). In addition, there is no geological line of evidence for chemical evolution of fluids with time. The cluster of data on the paired plot is in good agreement with the modal values of freezing point depression and homogenization temperature. As discussed later, the wide range of homogenization-temperatures is due to fluid pressure variation during the entrapment, although the effects of thermal re-equilibration due to stretching and undetectable necking cannot be ruled out completely.

9. Nature of syntectonic fluid

9.1. Salinity, composition, density and isochores

As the first melting of solid phases in most of the fluid inclusions occurred around 49 °C, it is evident that these fluid inclusions belong to the $CaCl_2$–NaCl–H_2O system. Projections of modal values of melting temperatures of last crystals of the hydrohalite ($T_{mh} = -31.8$ °C) and the ice ($T_{mi} = -17$ °C) on the triangular graph, H_2O–NaCl–$CaCl_2$, reveal that the wt. ratio of salts, NaCl/(NaCl +

Table 1
Summary of the important observations during freezing–heating experiments. All the fluid inclusions are secondary, occur in transgranular arrays, and contain two-phases (liquid/vapour) at room conditions

Observation	Inference	No. of observations	Temp. range (°C)	Modal temp. (°C)	Precision (°C)
Collapse of vapour bubble with sudden jerk	Complete freezing of the fluid phase (T_0)	81	−52.0 to −82	−65.0	±0.5
'Orange-peel' texture (characteristic granular appearance)	Distinct melting at a few degrees above the eutectic temperature (T_e)	78	−42 to −62	−49	+1.0
Sudden enhancement in the clarity of fluid inclusion/final melting of small euhedral grains	Final melting of hydrohalite (T_{mh})	45	−14 to −50	−32	±2.0
Melting of the last ice crystal	Freezing point depression (T_{mi})	114	−8 to −36	−17.0	±0.1
Disappearance of the vapour bubble	Homogenization into liquid-phase (T_h)	173	87.5 to 217.5	150	±0.1

Table 2
Summary of the results of paleostress analysis of different structures belonging to three phases. Φ—shape factor indicates relative amounts of principal stresses; RUP, ANG and COH are the indicators of the quality of solutions (see text for details)

	Structure	Method	σ_1-axis	σ_2-axis	σ_3-axis	Φ	RUP	ANG	COH (%)
First phase	Kinks	Ramsay (1962)	265°/00°	178°/00°	Subvertical	–	–	–	–
	Thrust	P–T axes	270°/08°	180°/05°	Subvertical	–	–	–	–
	Thrust	Dir inv	260°/00°	170°/10°	352°/80°	0.48	20	06°	86
Second phase	Faults and shear-zones	P–T axes	250°/10°	Vertical	160°/10°	–	–	–	–
		Dir inv	253°/04°	Vertical	163°/04°	0.35	19	13°	77
Third phase	Kinks	Ramsay (1962)	348°/05°	078°/00°	Vertical	–	–	–	–
	Thrust	P–T axes	350°/10°	078°/03°	Vertical	–	–	–	–
	Thrust	Dir inv	334°/03°	064°/03°	195°/85°	0.83	14	07°	98

$CaCl_2$), is 0.32 and the bulk salinity of the fluid is 19 wt.% NaCl + $CaCl_2$ (Oakes et al., 1990; Goldstein and Reynolds, 1994, p. 114). It is noteworthy that the values of salinity obtained by this graphical method compare closely (± 0.2 wt.%) with those yielded by the program *CalcicBrine* of Naden (1996). Substitutions of the molalities of NaCl and $CaCl_2$ and the range of homogenization temperature (154 ± 20 °C) in the equation given by Zhang and Frantz (1987) provide the density of the fluid as 0.9–1.0 g/cm^3, and the corresponding isochores.

9.2. Source of fluid

The highly saline, hot, dense and Ca-rich nature of the fluids implies that syntectonic brines are neither meteoric water, nor marine surface water, nor metamorphic water derived from dehydration of the Vindhyan sediments (Grant et al., 1990). The lack of acidic intrusives, either at local- or regional-scale, negates any possibility for magmatic origin of these fluids. The physico-chemical characteristics of the fluids are, however, consistent with connate or formational water origin. Several lines of geological evidence further support this interpretation. For example, without exception, the en-échelon veins in the sandstone beds are composed of quartz, whereas those in the limestone beds are composed of calcite. Strict lithological control on the composition of the vein-infillings, confinement of the veins within the individual beds and ubiquitous association of veins with pressure solution seams, all imply that the syntectonic fluids are the evolved connate waters that were derived from local and intraformational sources (Marquer and Burkhard, 1992).

Pressure-solution appears to be the dominant mechanism for generation of the mineralizing fluids in the host rocks. The drop in pressure due to fracturing results in a decrease in the solubility of silica and carbonates in the syntectonic brines (Srivastava and Engelder, 1991). Such a process must have been responsible for the precipitation of quartz and calcite in the fracture openings created during the brittle–ductile shearing. Generation and circulation of the mineralizing fluids was inhibited in the shale beds because of clayey composition and impermeability. The shale beds, therefore, lack veins despite being cut by several sets of abundant fractures.

10. Evidence for lithostatic pore-fluid pressure

The pore-fluid pressure conditions not only indicate the mechanism of fluid flow but also help constrain the trapping conditions from fluid inclusion data, particularly in situations where independent geothermometers or geobarometers are lacking. Since the fluid inclusion data reveal fluid pressure and not the rock pressure, it is crucial to ascertain whether the fluid pressure is due to hydrostatic or lithostatic load (Jenkin et al., 1994). The following lines of evidence suggest that the pore-fluid pressure achieved near-lithostatic to supralithostatic levels during the reactivation of the Great Boundary Fault. First, the compressional types of tectonic settings, revealed by paleostress analyses of the structures of all the three phases, indicate that the pore-fluid pressures were close to lithostatic pressure (Figs. 6, 9 and 10; Table 2). Second, the local and formational water origin of the syntectonic fluids and small size of the closed system, point to the lithostatic nature of pore-fluid pressure conditions. Third, occurrence of the impermeable shale beds at the tops and bottoms of both the Kaimur sandstone beds and the Nimbhahera limestone beds, and the confinement of the entire sedimentary sequence by peripheral faults and the basement granite must have been conducive for building-up lithostatic pore-fluid pressure. Finally, the lack of fractures or faults connecting the polyphase structures to the surface should rule out the possibility of hydrostatic pore-fluid pressure conditions.

11. Temperature and pressure of entrapment

Geothermal gradients in most sedimentary basins or diagenetic systems, vary between 20 and 50 °C/km (Mullis, 1979; Goldstein and Reynolds, 1994). If the average paleogeothermal gradient can be assumed as 35 °C/km, it is then possible to construct a thermobaric gradient, 1.32 °C/MPa, by using lithostatic geopressure gradient of 26.5 MPa/km. This thermobaric gradient intersects the isochores at points that define the entrapment conditions of syntectonic fluids at 195–270 °C and 129–185 MPa (Fig. 14). An important

implication of the trapping conditions, determined by this method, is the existence and denudation of a 5–7-km-thick column of overburden from the top of the Kaimur sandstone beds. Neither the occurrence of such a thick column of overburden is implied by any line of geologic evidence, nor is the prevalence of large-scale vertical movement of the crust resulting in uplift of lithosphere, rather than lateral motion of the plates during the Proterozoic era, established beyond doubt. The trapping conditions, inferred by assuming a geothermal gradient of 35 °C/km, are probably unrealistic.

Geological cross-sections and available stratigraphic data imply that the maximum possible thickness of overburden above the Kaimur sandstone was approximately 2 km in the Chittaurgarh region (Prasad, 1984; Sinha-Roy et al., 1986). The intersection of the 53 MPa isobaric line, corresponding to lithostatic pressure at a depth of 2 km, and the iscohores suggest that the trapping temperature was 160–202 °C. These trapping conditions reveal that the paleogeothermal gradient was of the order of 67.5–88.5 °C/km, that is, (160–25)/2 to (202–25)/2 °C/km, where 25 °C is the assumed surface temperature (Fig. 15).

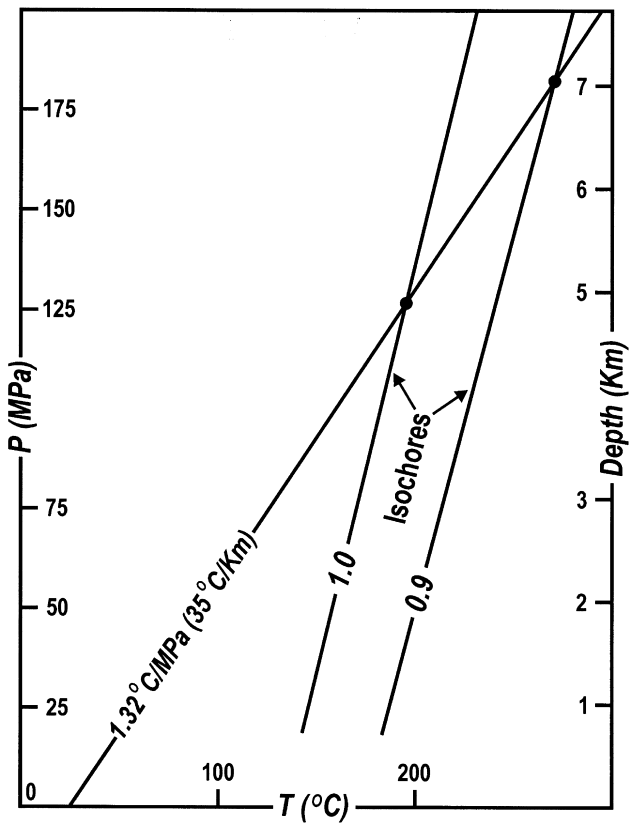

Fig. 14. P–T plot displaying isochores of 0.9 and 1.0 g/cm^3 densities corresponding to homogenization temperatures of 174 and 134 °C, respectively. These isochores would intersect the liquid-vapour curve at their respective homogenization temperatures (not shown in the figure). Thermobaric gradient is drawn for a geothermal gradient of 35 °C/km and a geopressure gradient of 26.5 MPa/km. The points of intersections of isochores with the thermobaric gradient constrain the lower and upper limits of the pressure and temperature of entrapment of the syntectonic fluid.

12. Discussion

12.1. High paleogeothermal gradient

Homogenization temperature, regardless of the pressure correction, gives the minimum estimate of trapping temperature. Heating experiments on the fluid inclusions occurring in syntectonic veins yield a homogenization temperature of 154 ± 20 °C, which is much higher than the temperature expected in a sedimentary formation of about 2 km burial depth (Fig. 13f). Such a condition is, however, not unique to the Vindhyan basin. Many recent studies on the Irish-type and Mississippi-Valley-type mineralization report the occurrence of anomalously high temperature fluid inclusions in the veins that are hosted by carbonate formations under shallow burial conditions (e.g. Kinsland, 1977; Friedman, 1987; Kontak and Sangster, 1995; Chi et al., 1998; Sangster et al., 1998). The occurrence of such a high temperature fluid inclusion population is commonly explained by any one or some combination of the following three factors. (i) Post-entrapment changes in the fluid inclusions (Roedder, 1984; Goldstein and Reynolds, 1994), (ii) mixing of formational fluids with high temperature fluids derived from locally anomalous heat sources, and (iii) entrapment of fluid inclusions in the geologic and tectonic settings of elevated geothermal gradients (Hitzman, 1995).

In this study, the effects of post-entrapment changes have been minimized by taking two precautions during the heating experiments. First, by analyzing the fluid inclusions exclusively in quartz, which is relatively less susceptible to thermal stretching than the carbonate minerals. Second, by restricting the measurement of homogenization temperatures on only those groups of fluid inclusions that show consistent liquid/vapour ratios. Existence of local heat sources is excluded by the geologic history of the area, and mixing of the connate fluid with the hot fluid of younger generation is not supported by any line of geologic evidence. By elimination, the elevated geothermal gradient could be the main cause for the entrapment of high temperature fluid inclusions during the development of syntectonic veins within the Vindhyan basin.

Fluid inclusion data obtained in this study indicate a paleogeothermal gradient of about 67.5–88.5 °C/km, which is ascribed to the continental rift type of tectonic setting of the Vindhyan basin and the Proterozoic age of the rifting process. Recent geophysical and geological studies confirm that the geological history of the Vindhyan basin begins with thinning of continental crust by stretching, rifting and basal volcanism during the Proterozoic era (Mishra et al., 1996; Ram et al., 1996; Raza and Casshyap, 1996). It is due to higher concentrations of radio isotopes, and more rapid and vigorous mantle convections during the Proterozoic era

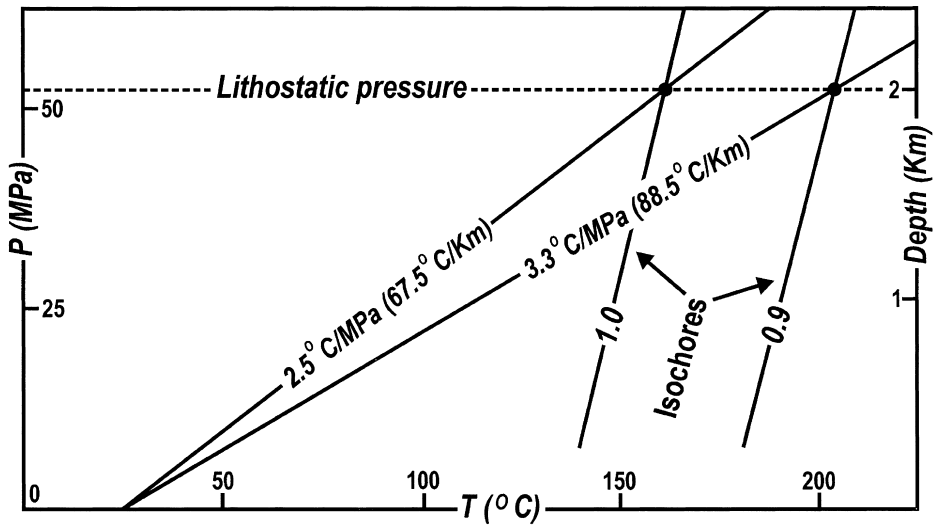

Fig. 15. P–T plot displaying 53 MPa isobaric line for lithostatic pressure at 2 km depth, and isochores of 0.9 and 1.0 g/cm^3 densities. The points of intersections of the isobaric line and isochores constrain P–T conditions for entrapment of the syntectonic fluid and imply paleogeothermal gradients of the order of 67.5–88.5 °C/km.

that the paleogeothermal gradients in the Proterozoic rift terrains would have been much more elevated than the present day geothermal gradients of 30–40 °C/km in the active continental rift terrains (Bridwell and Potzick, 1981).

In summary, the thinning of Proterozoic crust during continental rifting and the basal volcanism must have supplied necessary heat flux for setting-up of an elevated paleogeothermal gradient in the Vindhyan basin. The Berach granite, which is possibly a high heat producing basement granite, and the intermittent volcanism must have contributed as additional heat sources (Chakraborty et al., 1996). The geologic and tectonic settings of the Vindhyan basin were, therefore, conducive for building up an elevated geothermal gradient and entrapment of high temperature fluid inclusions.

12.2. Variation in pore-fluid pressure and mechanism of reactivation

The Great Boundary Fault developed initially as a steeply-dipping normal fault during the Proterozoic continental rifting, was reactivated as a reverse fault during the first event of seismic-slip. It is well known that the pore-fluid pressure must exceed the lithostatic pressure for reactivation of a normal fault into a reverse fault, provided the friction coefficient does not assume exceptionally low values (Sibson et al., 1988). That the condition of supralithostatic pore-fluid pressure, for reactivation of the Great Boundary Fault into a reverse fault, was satisfied during the first phase is evidenced by the occurrence of subhorizontal thrusts and flat veins in a tectonic setting of vertically directed minimum principal stress σ_3 (Table 2). Because of the total release of shear stress and sudden drop in the pore-fluid pressure during the post-seismic period of the first phase, the intermediate σ_2- and the minimum σ_3-principal stresses interchanged, and the thrust-type tectonic setting changed into a strike-slip type tectonic setting. This change in tectonic setting must have been facilitated by a low amount of differential stress and relatively high magnitudes of pore-fluid pressure. Similar interpretations regarding reactivation due to swapping of stress axes during the post-seismic period have been put forward by Boullier and Robert (1992), Cox (1995) and Henderson and McCaig (1996).

That the pore-fluid pressure was close to but less than the lithostatic pressure during the second event of the reactivation is indicated by the occurrence of numerous sub-vertical strike-slip faults and en-échelon veins of hybrid extensional-shear origin. This interpretation is consistent with the results of numerical modelling of Secor (1965) and Sibson (1996), who predict that strike-slip faulting in the earth's crust occurs at sublithostatic pore-fluid pressure conditions. Fluid inclusions in the second phase veins show a considerable range of homogenization temperatures, which is due to variation in the fluid pressure during entrapment of syntectonic fluids. The presence of crack-seal microstructures in syntectonic veins and the fluctuation in pore-fluid pressure shown by fluid inclusion data substantiate that the dilatancy or seismic pumping, driven by stress cycling in response to seismic activity on the Great Boundary Fault, was the dominant mechanism of fluid flow within the Vindhyan sedimentary rocks (cf. Sibson, 1989; Grant et al., 1990; Massonnet et al., 1996).

During the third phase of seismic-slip on the Great Boundary Fault, the pore-fluid pressure again achieved supralithostatic values, the minimum principal stress (σ_3) changed from horizontal to vertical, and the maximum compressive stress (σ_1) switched from E–W/horizontal to N–S/horizontal orientation. Consequently, a renewed reverse movement occurred on the Great Boundary Fault

and a new set of minor structures, namely, E–W-trending thrusts and kink folds developed, concomitantly.

In summary, the successive events of reactivation, related to seismic-slips on the Great Boundary Fault, are regarded as controlling the fluid pressure fluctuation and stress cycling in the Vindhyan rocks. Each major event of seismic-slip on the Great Boundary Fault triggered the establishment of a fluid pressure gradient, which resulted in rapid and focused flow of syntectonic fluids through high permeability channelways, namely, faults and fractures (Forster and Evans, 1991; Evans et al., 1997; Cox, 1999). Post-seismic drop in fluid pressure resulted in a decrease in solubility and deposition of silica and carbonate minerals within the fracture openings. With progressive decrease in the permeability of rupture zones, the fluid pressure increased to the levels of lithostatic or supralithostatic pressures and the conditions became favourable for the subsequent event of reactivation. The high temperatures preserved by the syntectonic fluid inclusions, the connate or formational water origin of the fluids, and the centimetre–metre scale of permeability zones, mean that the distance travelled by the syntectonic fluids was rather short and loss of temperature during the fluid migration was insignificant.

13. Conclusions

Successive events of reactivation or seismic-slip on the Great Boundary Fault are represented by distinct groups of minor structures in the Vindhyan sedimentary rocks. These minor structures serve as indicators of the pore-fluid pressure conditions and tectonic stresses. It is essentially due to supralithostatic pore-fluid pressure conditions that the Great Boundary Fault was reactivated as reverse fault during the first and the third events of reactivation, which occurred in plane deviatoric and axial extensional states of stress, respectively.

Due to the release of total shear stress and a sudden drop in pore-fluid pressure after the first event of reactivation, the intermediate principal stress σ_2 assumed a vertical orientation and a strike-slip type of movement marked the second event of reactivation on the Great Boundary Fault. The parallelism between the minimum principal stress σ_3 of the second phase and hinge lines of the first phase folds suggests that a significant axial extension of the first phase structures occurred during the second event of reactivation.

Fluid inclusion analyses reveal that the syntectonic fluids were essentially highly-dense Na–Ca–Cl brines of intraformational origin. Interpretation of fluid inclusion data, together with estimates of the thickness of overburden above the Kaimur sandstone beds imply that the strike-slip faulting occurred at 2 km depth, 53 MPa pressure and 160–202 °C temperature. These data point to a 67.5–88.5 °C/km paleogeothermal gradient, which is attributed to the continental rifting during the Proterozoic era, and the occurrence of additional heat sources, such as basal and intermittent volcanism and high heat-producing basement granite.

Although the first and second phase structures are developed abundantly in the Kaimur sandstone beds exposed around the Chittaurgarh area, these structures are not observed in the Lower Bhander Group rocks exposed in the Satur area (Fig. 1). The first and second events of reactivation on the Great Boundary Fault can, therefore, be inferred to have occurred between 750 and 900 Ma, which are probable ages of the Bhander Group and the Kaimur Group, respectively (Venkatachala et al., 1996; Ray et al., 2002). As the Lower Bhander Group is also the youngest stratigraphic horizon bearing the imprints of the third phase structures, the third event of reactivation must be younger than 750 Ma. The upper limit for the age of the third event is difficult to ascertain due to lack of geochronological data for a substantial section of the Vindhyan sequence.

Acknowledgements

Constructive reviews by Anne-Marie Boullier, the anonymous referee, Richard Norris, Ramesh Chander, Biswajit Mishra, O.P. Varma and Rajesh Sharma helped improve the manuscript considerably. Dr Boullier was generous enough to clarify a couple of points at the post-review stages. Rakesh Kumar Singh helped during the microthermometric experiments. D.K. Mukhopadhyay, A.K. Sen and A.K. Pachauri offered several suggestions during the revision of the manuscript. This work is funded by 'Deep Continental Studies Program' of the DST (Govt. of India), UGC 'Research Award' scheme and AICTE project. Amit Sahay is supported by CSIR, Senior Research Fellowship.

References

Angelier, J., 1990. Inversion of field data in fault tectonics to obtain the regional stress. III. A new rapid direct inversion method by analytical means. Geophysical Journal International 103, 363–376.

Angelier, J., 1994. Fault slip analysis and paleostress reconstruction. In: Hancock, P.L., (Ed.), Continental Deformation, Pergamon Press, Oxford, pp. 53–100.

Banerjee, A.K., Singh, M.H.J., 1981. Palaeogeography and sedimentation of Vindhyans in eastern Rajasthan. Miscellaneous Publication of Geological Survey of India 50, 89–94.

Banerjee, A.K., Sinha, P.N., 1981. Structure and Tectonics of Vindhyans in Eastern Rajasthan. Miscellaneous Publication of Geological Survey of India 50, 41–47.

Boullier, A.M., Robert, F., 1992. Palaeoseismic events recorded in Archaean gold-quartz vein networks, Val d'Or, Abitibi, Quebec, Canada. Journal of Structural Geology 14, 161–179.

Bridwell, R.J., Potzick, C., 1981. Thermal regimes, mantle diapirs and crustal stresses of continental rifts. Tectonophysics 73, 15–32.

Chakraborty, P.P., Banerjee, C., Das, N.G., Sarkar, S., Bose, P.K., 1996. Volcaniclastics and their sedimentological bearing in Proterozoic Kaimur and Rewa Groups in central India. Memoir Geological Society of India 36, 59–75.

Chi, G., Kontak, D.J., Williams-Jones, A.E., 1998. Fluid composition and thermal regime during Zn–Pb mineralisation in the Lower Windsor Group, Nova Scotia, Canada. Economic Geology 93, 883–895.

Cox, S.F., 1995. Faulting processes at high fluid pressures: an example of fault valve behavior from the Wattle Gully Fault, Victoria, Australia. Journal of Geophysical Research 100 (B7), 12841–12859.

Cox, S.F., 1999. Deformational controls on the dynamics of fluid flow in mesothermal gold systems. In: McCafrey, K.J.W., Lonergan, L., Wilkinson, J.J. (Eds.), Fractures, Fluid Flow and Mineralisation. Geological Society, London, Special Publications 155, pp. 123–140.

Davis, D.W., Lowenstein, T.K., Spencer, R.J., 1990. Melting behavior of fluid inclusions in laboratory-grown halite crystals in the systems $NaCl–H_2O$, $NaCl–KCl–H_2O$, $NaCl–MgCl_2–H_2O$ and $NaCl–CaCl_2–H_2O$. Geochimica et Cosmochimica Acta 54, 591–601.

Evans, J.P., Forster, C.B., Goddard, J.V., 1997. Permeability of fault-related rocks, and implications for hydraulic structure of fault zones. Journal of Structural Geology 19, 1393–1404.

Fermor, L.L., 1930. On the age of Aravalli Range. Record, Geological Survey of India 62 (4), 391–409.

Forster, C.B., Evans, J.P., 1991. Hydrogeology of thrust and crystalline thrust sheets: results of combined field and modeling studies. Geophysical Research Letter 18 (5), 979–982.

Friedman, G.M., 1987. Deep-burial diagenesis: its implication for vertical movements of crust, uplift of the lithosphere and isostatic unroofing—a review. Sedimentary Geology 50, 67–94.

Goldstein, R.H., Reynolds, T.J., 1994. Systematics of fluid inclusions in diagenetic minerals. SEPM Short Course 31, Society of Sedimentary Petrology, Oklahoma, USA, 198pp.

Grant, N.T., Banks, D.A., McCaig, A.M., Yardley, B.W.D., 1990. Chemistry, source and behavior of fluids involved in Alpine thrusting of the Central Pyrenees. Journal of Geophysical Research 95 (B6), 9123–9131.

Henderson, I.H.C., McCaig, A.M., 1996. Fluid pressure and salinity variations in shear zone-related veins, central Pyrenees, France: implications for the fault-valve model. Tectonophysics 262, 321–348.

Heron, A.M., 1953. The Geology of central Rajputana. Memoir Geological Survey of India 79 (1), 1–389.

Hitzman, M.W., 1995. Mineralization in the Irish Zn–Pb–(Ba–Ag) orefield. Society of Economic Geologists. Guide Book Series 21, 25–61.

Iqbaluddin, Prasad, B., Sharma, S.B., Mathur, R.K., Gupta, S.N., Sahai, T.N., 1978. Genesis of the Great Boundary Fault of Rajasthan, India. Proceedings of the Third Regional Conference on Geology and Mineral Resources of South-East Asia, Bangkok, pp. 145–149.

Janssen, C., Michel, G.W., Bau, M., Luders, V., Muhle, K., 1997. The north Anatolian Fault Zone and the role of fluids in seismogenic deformation. Journal of Geology 105, 387–403.

Jenkin, G.R.T., Craw, D., Fallick, A.E., 1994. Stable isotopic and fluid inclusion evidence for meteoric fluid penetration into an active mountain belt; Alpine Schist, New Zealand. Journal of Metamorphic Geology 12, 429–444.

Kinsland, G.L., 1977. Formation temperature of fluorite in the Lockport Dolomite in Upper New York State as indicated by fluid inclusion studies—with discussion of heat sources. Economic Geology 72, 849–854.

Kontak, D.J., Sangster, D.F., 1995. Aqueous and liquid petroleum inclusions in barite from the Walton deposit, Nova Scotia: a Carboniferous, carbonate-hosted Ba–Pb–Zn–Cu–Ag deposit. Economic Geology 93, 845–868.

Lespinasse, M., 1999. Are fluid inclusion planes useful in structural geology. Journal of Structural Geology 21, 1237–1243.

Lespinasse, M., Pecher, A., 1986. Microfracturing and regional stress field: a study of the preferred orientation of fluid-inclusion planes in a granite from the Massif Central, France. Journal of Structural Geology 8, 169–180.

Marquer, D., Burkhard, M., 1992. Fluid circulation, progressive deformation and mass-transfer processes in the upper crust: the example of basement-cover relationships in the External Crystalline Massifs, Switzerland. Journal of Structural Geology 14, 1047–1057.

Massonnet, D., Thatcher, W., Vadon, H., 1996. Detection of postseismic fault-zone collapse following the Landers earthquake. Nature 382, 612–616.

Means, W.D., Li, T., 2001. A laboratory simulation of fibrous veins: some first observation. Journal of Structural Geology 23, 857–863.

Mishra, D.C., Gupta, S.B., Vyaghreswara, R., Venkatrayudu, M., 1996. Crustal structure and basement tectonics under Vindhyan basin: gravity–magnetic study. Memoir Geological Society of India 36, 213–224.

Mullis, J., 1979. The system methane-water as a geologic thermometer and barometer from the external part of the central Alps. Bulletin de Mineralogie 102, 526–536.

Naden, J., 1996. CalcicBrine 1.5: a Microsoft Excel 5.0 add-in for calculating salinities from microthermometric data in the system $NaCl–CaCl_2–H_2O$. PACROFI VI, University of Wisconsin (abs).

Oakes, C.S., Bodnar, R.J., Simonson, J.M., 1990. The system $NaCl–CaCl_2–H_2O$, I. The ice liquidus at 1 atm total pressure. Geochimica et Cosmochimica Acta 54, 603–610.

Pascoe, E.H., 1959. A Manual of Geology of India and Burma II. Government of India Press, Calcutta.

Prasad, B., 1984. Geology, sedimentation and paleogeography of the Vindhyan Supergroup, south-eastern Rajasthan. Memoir Geological Survey of India 116 (1), 1–107.

Ragan, D.M., 1985. Structural Geology: An Introduction to Geometrical Techniques, 3rd ed, John Wiley & Sons, New York.

Ram, J., Shukla, S.N., Pramanik, A.G., Varma, B.K., Chandra, G., Murthy, M.S.N., 1996. Recent investigations in the Vindhyan basin: implications for the basin tectonics. Memoir Geological Society of India 36, 267–286.

Ramsay, J.G., 1962. Geometry of conjugate fold systems. Geological Magazine 99, 516–526.

Ramsay, J.G., 1980. The crack-seal mechanism of rock deformation. Nature 284, 135–139.

Ray, J.S., Martin, M.W., Veizer, J., Bowring, S.A., 2002. U–Pb zircon dating and Sr isotope systematics of the Vindhyan Supergroup, India. Geological Society of America 30 (2), 131–134.

Raza, M., Casshyap, S.M., 1996. A tectono-sedimentary model of evolution of middle Proterozoic Vindhyan basin. Memoir Geological Society of India 36, 287–300.

Roedder, E., 1984. Fluid inclusions. Mineralogical Society of America. Reviews in Mineralogy 12.

Sangster, D.F., Savard, M.M., Kontak, D.J., 1998. A genetic model for mineralisation of Lower-Windsor (Visean) carbonate rocks of Nova Scotia, Canada. Economic Geology 93, 932–952.

Secor, D.T., 1965. Role of fluid pressure in jointing. American Journal of Science 263, 633–646.

Sibson, R.H., 1989. Earthquake faulting as a structural process. Journal of Structural Geology 11, 1–14.

Sibson, R.H., 1996. Structural permeability of fluid-driven fault-fracture meshes. Journal of Structural Geology 18, 1031–1042.

Sibson, R.H., Robert, F., Poulsen, K.H., 1988. High-angle reverse faults, fluid-pressure cycling, and mesothermal gold-quartz deposits. Geology 16, 551–555.

Sinha-Roy, S., Kirmani, I.R., Reddy, B.V.R., Sahu, R.L., Patel, S.N., 1986. Fold pattern in the Vindhyan sequence in relation to Great Boundary Fault: example from Chittaurgarh area, Rajasthan. Quaternary Journal of Geological Mining and Metallurgical Society of India 58 (4), 241–251.

Sinha-Roy, S., Malhotra, G., Guha, D.B., 1995. A transect across Rajasthan Precambrian terrain in relation to geology, tectonics and crustal evolution of south-central Rajasthan. Memoir Geological Society of India 31, 63–89.

Srivastava, D.C., Engelder, T., 1990. Crack-propagation sequence and pore-fluid conditions during fault-bend folding in the Appalachian

Valley and Ridge, central Pennsylvania. Geological Society of America Bulletin 102, 116–128.

Srivastava, D.C., Engelder, T., 1991. Fluid evolution history of brittle–ductile shear zones on the hanging wall of Yellow Spring thrust, Valley and Ridge Province, Pennsylvania, USA. Tectonophysics 198, 23–34.

Srivastava, D.C., Lisle, R.J., Vandycke, S., 1995. Shear zones as a new type of paleostress indicator. Journal of Structural Geology 17, 663–676.

Srivastava, D.C., Lisle, R.J., Imran, M., Kandpal, R., 1999. A new approach for paleostress analysis from Kink Bands: application for fault-slip methods. Journal of Geology 107, 165–176.

Tiwari, S., 1995. Extension of the Great Boundary Fault (GBF) of Rajasthan in the Ganga Valley. Memoir Geological Society of India 31, 311–328.

Turner, F.J., 1953. Nature of dynamic interpretation of deformation lamellae in calcite of three marbles. American Journal of Science 251, 276–298.

Venkatachala, B.S., Sharma, M., Shukla, M., 1996. Age and life of the Vindhyans—facts and conjectures. Memoir Geological Society of India 36, 137–165.

Verma, P.K., 1996. Evolution and age of the Great Boundary Fault of Rajasthan. Memoir Geological Society of India 36, 197–212.

Vrolijk, P., 1987. Tectonically-driven fluid flow in the Kodiak accretionary complex, Alaska. Geology 15, 466–469.

Zhang, Y., Frantz, J.D., 1987. Determination of the homogenization temperatures and densities of supercritical fluids in the system NaCl–KCl–$CaCl_2$–H_2O using synthetic fluid inclusions. Chemical Geology 64, 335–350.

Zulauf, G., Duyster, J., 1997. Faults and veins in the superdeep well KTB: constraints on the amount of Alpine intra-plate thrusting and stacking of Variscan basement (Bohemian Massif, Germany). Geologische Rundschau 86S, S28–S33.